Solar-driven membrane distillation with direct ambient-temperature feed heating: design, modeling, and experimental validation

Original
Solar-driven membrane distillation with direct ambient-temperature feed heating: design, modeling, and experimental validation / Morosanu, S., Morciano, M.. - In: DESALINATION. - ISSN 0011-9164. - 620:(2026). [10.1016/j.desal.2025.119660]

Publisher:
ELSEVIER

Published
DOI:10.1016/j.desal.2025.119660

Desalination 620 (2026) 119660

Contents lists available at ScienceDirect

Desalination

journal homepage: www.elsevier.com/locate/desal

Solar-driven membrane distillation with direct ambient-temperature feed heating: design, modeling, and experimental validation

Stefan Morosanu [a,b], Matteo Morciano [a,c,*]

[a] Department of Energy, Politecnico di Torino, Corso Duca degli Abruzzi 24, 10129 Torino, Italy
[b] Green Independence S.R.L., Piazza del Popolo 1, 72100 Brindisi, Italy
[c] Clean Water Center, Politecnico di Torino, Corso Duca degli Abruzzi 24, 10129 Torino, Italy

HIGHLIGHTS

- Compact DCMD powered by distributed solar energy with ambient-temperature feed.
- Experimentally demonstrated direct feed heating via integrated flat solar absorber.
- Validated a CFD model accurately predicting system performance.
- Achieved 0.51 ± 0.02 LMH distillate flux under 1 sun, with salt rejection >99.9%.
- Proposed a novel internal heat recovery layout enhancing distillate flux.

ARTICLE INFO

Dataset link: Raw experimental data (Original data)

Keywords:
Desalination
Membrane distillation
Renewable energy
Solar energy
Sustainability

ABSTRACT

Freshwater scarcity in off-grid regions necessitates the development of simple and sustainable desalination systems. Conventional membrane distillation (MD), while promising, typically relies on external preheating and complex solar collectors, limiting its compactness and practical applicability. This study presents the design, numerical modeling, and experimental validation of a compact direct contact MD prototype powered exclusively by distributed solar energy. The system operates without external feedwater preheating or centralized solar collectors. Instead, the custom-built module integrates a solar absorber directly into the top surface of the feed channel, enabling direct solar heating of the ambient-temperature feed stream. The flat-sheet module employs reduced channel thickness to enhance thermal coupling and minimize temperature polarization. An extensive experimental campaign was conducted under realistic conditions, covering a broad range of feed flow rates. A numerical model was developed to simulate coupled heat and mass transfer processes, and validated against experimental results, showing strong agreement. The model was subsequently used to explore alternative configurations and guide system optimization through internal heat recovery. A promising thermal management strategy is thus introduced, enabling simultaneous feed preheating and permeate cooling, thus increasing effective transmembrane temperature difference without additional energy input. A maximum distillate flux of 0.51 ± 0.02 kg m^{-2} h^{-1} was achieved under 1000 W m^{-2} solar irradiation, representing 59% improvement over comparable tested systems lacking internal heat recovery. Results demonstrate the feasibility of a modular and scalable system suitable for off-grid or decentralized water purification. Future work will investigate multistage implementations and integration with alternative low-grade heat sources.

1. Introduction

Water scarcity and climate change are two of the most pressing global challenges faced today [1,2]. Nowadays, about 4 billion people experience water scarcity to some degree, and this number is expected to grow to around 6 billion by 2050 [3] due to factors such as population growth, industrial demand, and the degradation of water resources [4]. At the same time, the need to decarbonize energy systems in response to climate change [5] is drawing increasing attention to water treatment technologies powered by renewable energy sources [6]. Therefore, integrating renewable energy sources into water treatment technologies is essential to mitigate climate impacts and provide sustainable access to fresh water [7].

Among the various renewable sources, solar energy is the most abundant. Each year, the Earth receives more than a thousand times the

---

[*] Corresponding author at: Department of Energy, Politecnico di Torino, Corso Duca degli Abruzzi 24, 10129 Torino, Italy.
E-mail address: matteo.morciano@polito.it (M. Morciano).

https://doi.org/10.1016/j.desal.2025.119660
Received 17 October 2025; Received in revised form 14 November 2025; Accepted 17 November 2025

total global energy consumption in the form of solar radiation [8,9]. However, its relatively low power density often limits its application in energy-intensive processes. Membrane distillation (MD), a thermally driven separation process capable of operating with low-grade heat [10], is particularly well-suited for coupling with solar energy to produce fresh water [11]. Numerous studies have explored the integration of MD with solar energy [12]. Conventional systems typically rely on thermal energy storage [13], requiring multiple components such as solar collectors [14], storage tanks, and heat exchangers. A commonly investigated configuration is the integration of a flat-plate solar collector with a thermal energy storage unit and a MD module. For example, Boubakri et al. [15] developed and experimentally tested a solar-powered direct contact MD (DCMD) plant comprising four main subsystems: a 20 m^2 solar collector, a 1.48 kW peak PV system, three DCMD modules (3.39 m^2 total), and a 103 L h^{-1} cooling circuit. They reported distillate production rates up to 4.59 L h^{-1} per module, and a minimum STEC of 1609 kWh m^{-3}, highlighting the potential of integrating solar energy with DCMD.

Recent research trends have increasingly focused on developing more compact [16], integrated devices that employ direct solar heating [17]. Indeed, solutions in which the solar collector/absorber is directly integrated into the MD unit have been explored [18]. These approaches aim to improve overall system efficiency by reducing heat losses associated with extended module length, piping and auxiliary components. Nonetheless, most of the literature to date has focused on passive compact devices, where feedwater transport occurs via capillary action [18] and the system operates without external pumps or active flow control [19]. These systems offer several advantages, including high specific distilled water productivity, simplified construction due to the absence of sealing elements and active flow regulation components, and autonomous operation. However, they also suffer from critical limitations, such as geometric constraints [20] (e.g., dry-out issues occur when the capillary path exceeds approximately 10–16 cm [21]), limited operational flexibility, and the progressive accumulation of salt within the hydrophilic material. These drawbacks significantly restrict the scalability and long-term reliability of passive systems. One promising strategy to address these challenges and thus mitigate the scalability problem of passive configurations is the design of active MD systems powered by distributed solar energy.

To the best of our knowledge, only a few active systems have been developed that operate solely using solar energy distributed along the feed channel and directly absorbed by the feedwater, i.e., based on direct (surface) heating [22,23]. These efforts can be broadly categorized into two types. The first type includes photothermal membrane distillation (PTMD) devices [24], which integrate solar-absorbing materials on the hydrophobic side of the membrane to achieve localized heating [25] of the feed side. However, these absorption layers often suffer from degradation phenomena such as detachment, nanoparticle dislodgement, and membrane fragility, ultimately compromising system integrity and performance [22]. Furthermore, PTMD systems cannot effectively utilize distributed waste heat in forms other than direct solar irradiation. The second type encompasses active compact systems that exploit distributed solar energy [26,27] or waste heat [28], such as that from photovoltaic modules, without relying on photothermal coatings. For example, one study investigated an air-gap membrane distillation (AGMD) module integrated with PV panels [28]. Despite these efforts, active MD systems that operate exclusively with distributed solar energy along feed channel and ambient-temperature feedwater (i.e., without external or initial preheating), remain poorly explored from both experimental and modeling perspectives.

A comprehensive overview of interfacial heating approaches in membrane distillation was recently provided by Hu et al. [29], who categorized the main heating strategies, including photothermal, Joule, induction, and conduction heating, and discussed their potential to mitigate temperature polarization while improving energy efficiency. These methods generally rely on localized heat generation at or near the membrane surface through advanced functional materials or electrical inputs, offering valuable insight into emerging in-situ heating concepts. Beyond this broad classification, the review also provides a systematic and quantitative comparison of performance metrics, together with a forward-looking discussion on key research directions, including hybrid heating strategies, advanced CFD modeling, and the development of durable self-heating materials. These perspectives highlight the growing interest in compact and energy-efficient desalination technologies and reinforce the relevance of exploring alternative low-temperature configurations.

In this study, we propose and investigate a novel, compact flat-sheet DCMD module that integrates a solar absorber directly onto its upper surface. The system operates without any external or initial preheating of the feedwater and employs active circulation via a pump, allowing precise control of flow rates, improved thermal management, and reduced temperature polarization. The entire module was custom-designed and fabricated to match the specific operating conditions of interest, namely, ambient-temperature feedwater and the exclusive use of distributed solar heat. Operating under such low inlet temperature conditions is particularly relevant from an energetic and practical standpoint: direct heating within the MD module minimizes energy losses associated with external preheating and transport, simplifies system design and minimizes usage of hardware, and allows autonomous operation under variable solar irradiation. These features make the configuration especially suitable for small-scale, off-grid, or resource-limited applications. To further enhance performance under low driving temperature differences, both feed and permeate channels were designed with reduced and optimized thicknesses, improving heat and mass transfer while maximizing system compactness and efficiency. Furthermore, a novel configuration incorporating an internal heat-recovery mechanism was introduced, in which an auxiliary feed channel located beneath the permeate stream passively preheats the incoming feed while concurrently cooling the permeate. To thoroughly characterize the performance of the proposed prototype, we conducted an extensive experimental campaign that covered a wide range of operating conditions. This included varying the feed and permeate flow rates and evaluating multiple system configurations. The experiments provided a detailed assessment of transmembrane vapor flux, thermal efficiency, and salt rejection under realistic solar-driven operating scenarios. In parallel, we developed a numerical model of the system to simulate the coupled heat and mass transfer phenomena. The model was validated against the experimental results and then used to extrapolate performance beyond the tested conditions and to identify optimal thermal management strategies. By combining custom device design, experimental validation, and numerical optimization, this work contributes to a comprehensive and scalable solution for solar-driven water treatment based on compact and flexible MD technology. Moreover, it enhances the fundamental understanding of systems operating with direct solar heating and low inlet feed temperatures. These findings aim to support the development and deployment of such solutions in settings where limited infrastructure or resource constraints require efficient and low-temperature processes.

2. Methods

2.1. Description of the designed prototype

The prototype developed for this study draws inspiration from compact and passive MD systems powered by distributed solar energy, as explored and investigated in previous works [18,19]. However, in contrast to those passive systems, the present work focuses on a active compact device equipped with pumps to control and fine-tune the mass flow rates in both the feed and permeate channels. The system features a flat-sheet membrane configuration, with solar heating distributed directly along the feed channel to enhance thermal coupling. The main components of the device under investigation are illustrated in Fig. 1.

The module, consists of two separate water channels: a feed channel containing seawater and a permeate channel containing distilled water. Each channel has a height 2.60 mm. These are separated by a hydrophobic polytetrafluoroethylene (PTFE) membrane with a thickness of $h = 0.18 \pm 0.05$ mm, an average porosity of $\epsilon = 0.81$, and an average pore size of $d_p = 0.45$ μm. The choice of a 2.60 mm channel height represents a compromise between practical manufacturability and improved thermal coupling under low-temperature, distributed solar heating. Conventional DCMD modules often use larger channel heights, suitable for externally preheated feedwater but prone to thermal polarization under small driving temperature differences. Reducing the channel height in the present design minimizes conductive and convective losses, enhancing heat transfer efficiency and maximizing the effective transmembrane temperature difference. Preliminary simulation results conducted at low mass flow rate (5.60 mL min^{-1}) indicated reducing the channel height to 1 mm would increase distillate flux by only about 10%. Although thinner channels can enhance performance by improving heat and mass transfer, heights below 2.60 mm were deemed impractical due to fabrication constraints, increased pressure losses, and potential mechanical instability. This analysis justifies the selected channel height, which represents an effective trade-off between performance, structural robustness, and suitability for distributed solar operation. Both channels are equipped with spacers to maintain structural integrity and ensure proper membrane alignment. The footprint of the module is 36 × 36 cm. Mass transfer occurs via vapor diffusion across the membrane, driven by the vapor pressure difference generated by the temperature gradient between the feed and permeate streams. To establish this gradient using only distributed solar energy, a custom integrated solar absorber was developed. It consists of an aluminum plate coated on the top surface with a high-absorption layer (commercially known as TINOX) characterized by a high solar absorbance ($\alpha_c = 0.95$) and low infrared emissivity ($\epsilon_c = 0.04$). An 8 mm thick polycarbonate plate is placed on top of the absorber to reduce convective heat losses to the environment and to shield the surface from dust and debris. The uncoated back side of the aluminum plate is in direct thermal contact with the feed channel, thereby transferring absorbed solar energy to the feedwater and establishing the temperature difference required for transmembrane vapor flux. A metal cooling plate with circulating water is employed as a heat sink on the permeate side to maintain the thermal gradient [13,28]. This component is represented in Figs. 1a and b and 3 as the heat exchanger.

The entire device was custom-designed from scratch, with optimized feed and permeate channel thicknesses to suit the low-temperature gradients expected in distributed direct solar heating scenarios. The reduced thickness of the channels improves heat and mass transfer while minimizing thermal losses, making the system more effective under the specific operating conditions of interest (i.e., no initial and external preheating and reliance solely on solar-distributed heat). Interestingly, in this study, we also propose an alternative and more efficient approach that eliminates the need for an external cooling plate and associated chiller. The proposed design incorporates an auxiliary channel located beneath the permeate side where feedwater flows, which functions as a heat sink for the permeate while simultaneously preheating the incoming feed. This configuration improves internal heat recovery and, consequently, enhances thermal management and overall system efficiency by redirecting energy that would otherwise be dissipated. Extensive technical details on the thermal architecture and flow configurations are presented in the following subsection.

2.1.1. Device layouts and operating configurations

Four specific layouts of the DCMD device were investigated to develop a comprehensive understanding of its behavior under distributed direct solar energy and low-temperature feedwater conditions. In all the configurations, the inlet temperature of the permeate stream was indeed maintained at 20 °C. The different configurations analyzed in this study are illustrated in Fig. 2, where the arrows denote flow directions. The configurations are referred to as follows:

- PF (parallel flow, panel a): Both feed and permeate inlets are maintained at 20 °C, with streams flowing in the same direction. This setup represents a conventional DCMD baseline, here tested under the unconventional regime of distributed solar heating and low mass flow rates.
- CF (counter flow, panel b): Similar to PF, but with opposite flow directions for feed and permeate. This arrangement is the standard benchmark in MD literature due to its improved driving temperature profile compared to PF, under conventional operating conditions.
- $CF_{f,\ closed-loop}$ (feed in a closed loop, panel c): This configuration features a thermally closed-loop feed circuit. In this setup, only the inlet temperature of the permeate stream is maintained at 20 °C, while the feed inlet temperature is left uncontrolled. As a result of continuous solar energy input (I_{solar}) and thermal buffering effect provided by the feed tank, the feed temperature increases progressively during operation, often exceeding 20 °C. This setup allows the evaluation of system behavior under more realistic and unconstrained solar heating conditions. A countercurrent flow arrangement, identical to that used in CF (see Fig. 2b), is adopted here.
- $CF_{heat\ recovery}$ (panel d): A modified counterflow layout in which the permeate stream is cooled and the feed preheated via an auxiliary channel located beneath the permeate channel, separated by a thin aluminum plate. This design simultaneously cools the permeate and preheats the feed without the need for an external chiller or heat exchanger, thereby reducing hardware requirements and enabling a more standalone operation. In detail, in this configuration both the feed and permeate inlet temperatures are set to be 20 °C, similar to baseline configuration. However, this configuration introduces a modified layout aimed at optimizing thermal management. The core objective is to recover the heat flux that would otherwise be dissipated to the sink (namely $\phi_{\text{heat sink}}$, see Fig. 1b) and use it to preheat the feed stream. To ensure effective thermal coupling, an auxiliary channel portion where feedwater flows is placed beneath the permeate channel (see Fig. 2d), separated by a 1 mm thick aluminum plate to facilitate efficient heat transfer. This design serves a dual purpose: it cools the permeate while simultaneously preheating the feed, thus improving overall system energy efficiency. In this setup, external cooling is not required. Thus the heat exchanger (component 8 in Fig. 1a) and related chiller are removed. Additionally, the aluminum plate on the bottom side is replaced with a 12 mm thick PTFE plate, which provides thermal insulation and structural support.

A comparative summary of their key characteristics is also reported in Table 1. Overall, the PF and CF layouts, which rely on active external cooling, primarily serve as reference benchmarks for controlled testing. The $CF_{f,\ closed-loop}$ configuration reproduces more realistic solar-driven operation, in which the feed temperature progressively increases during operation; this enhances productivity but results in less stable inlet conditions. In addition, in a real-scale closed-loop application, the feed salinity would need to be carefully monitored to prevent concentration buildup. Finally, the $CF_{heat\ recovery}$ configuration has the potential to achieve the highest thermal efficiency by internally recovering heat that would otherwise be lost, at the cost of incorporating an auxiliary, yet fully integrated, channel. This layout highlights the potential for compact, passive, and energy-efficient operation without the need for external heat exchangers.

2.2. Experimental setup

The experimental setup used in this study is illustrated in Fig. 3. This setup was designed to evaluate the specific mass flow rate of distilled water through the membrane, denoted as J and expressed in

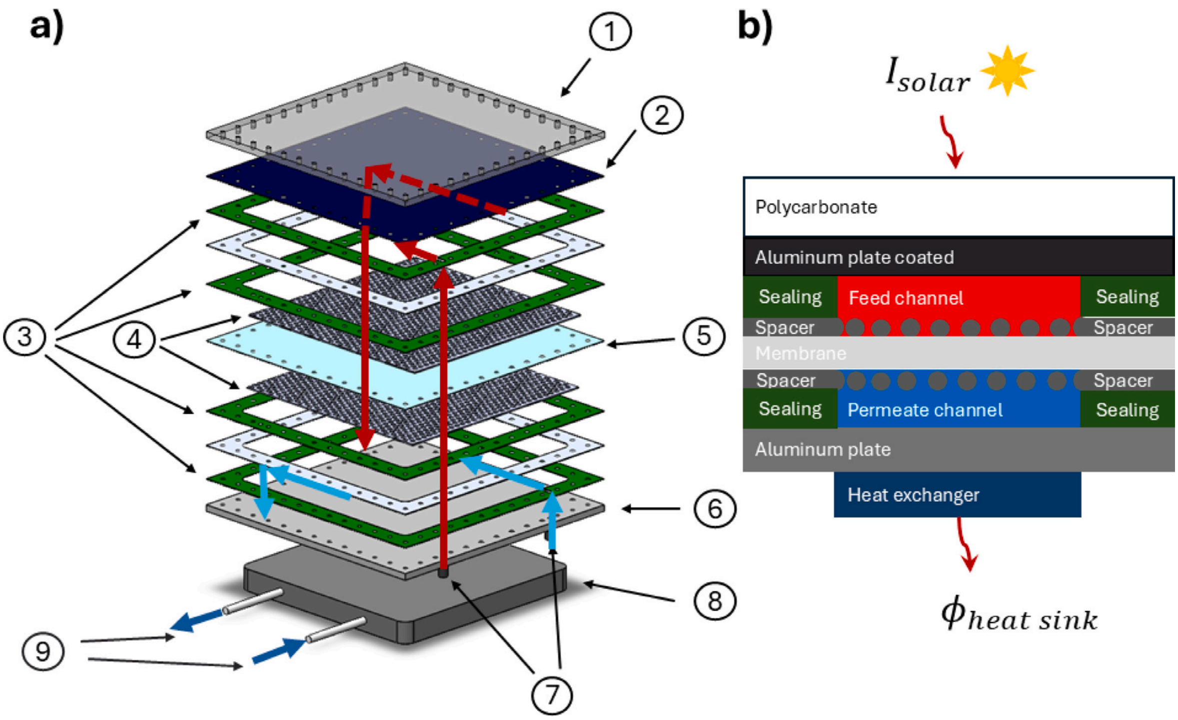

Fig. 1. Schematic representation of the prototype investigated in the study. (a) CAD rendering of the main components: (1) polycarbonate cover, (2) coated aluminum plate solar absorber, (3) sealing gaskets, (4) spacers, (5) PTFE membrane, (6) aluminum plate, (7) feed and permeate inlets, (8) heat exchanger (HEX) and (9) cooling water inlet and outlet of heat exchanger. (b) Cross-sectional schematic of the assembled device. The red and blue areas represent the feed and permeate channels, respectively.

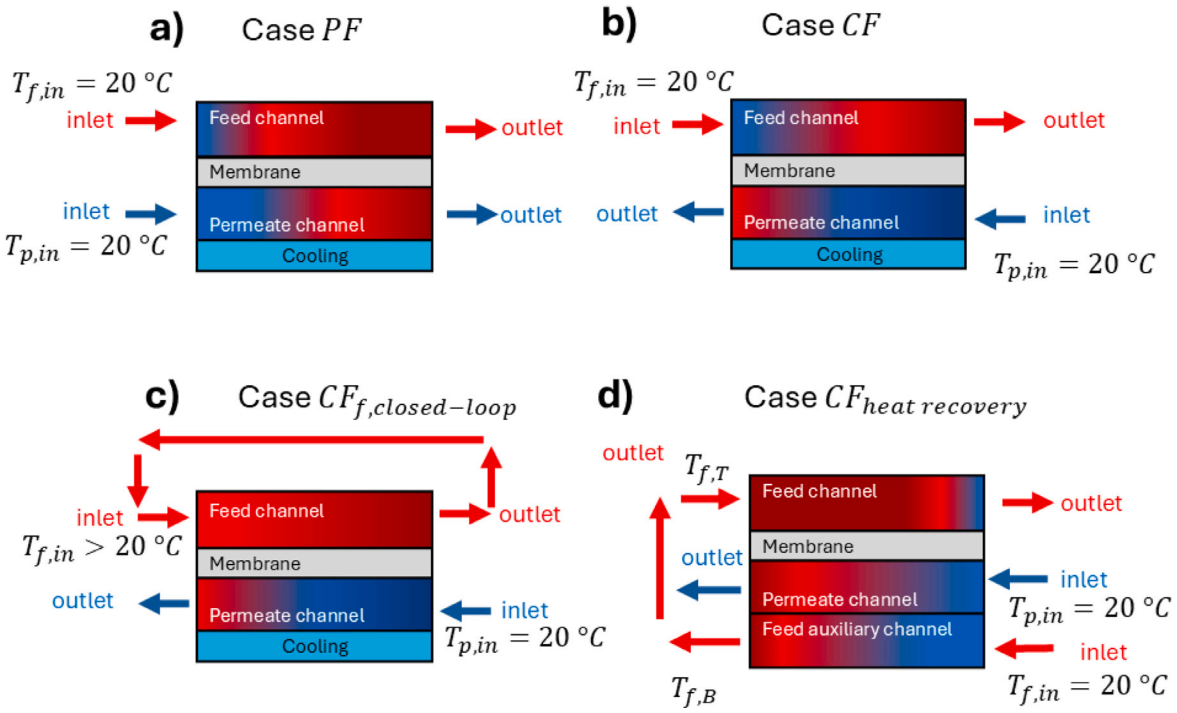

Fig. 2. Schematic of the tested configuration. Panels (a), (b), (c) and (d) show cross-sectional views of the four configurations analyzed: PF, CF, $CF_{f,\ closed-loop}$, and $CF_{heat\ recovery}$, respectively. Red arrows indicate feed-side flow paths; blue arrows indicate permeate-side flow paths. Note that, the terms $T_{f,T}$ and $T_{f,B}$ reported in panel (d) refer to the temperature of the fluid at the inlet of the feed channel, placed on top of the module, and at the outlet of the auxiliary feed channel, placed at the bottom of the module (beneath the permeate channel), respectively. $T_{f,in}$ and $T_{p,in}$ refer to the temperature of the feed and permeate streams entering the module, respectively.

Table 1

Summary of tested DCMD configurations and their main operating features.

Configuration	$T_{f,in}$	$T_{p,in}$	Flow direction	Cooling method	Note
PF	20 °C	20 °C	Co-current	Active (HEX+chiller)	Baseline case
CF	20 °C	20 °C	Counter-current	Active (HEX+chiller)	Baseline case
$CF_{f,\ closed-loop}$	>20 °C	20 °C	Counter-current	Active (HEX+chiller)	No feed thermalization
$CF_{heat\ recovery}$	20 °C	20 °C	Counter-current	Internal heat recovery	Aux. channel, no HEX

kg m^{-2} h^{-1}. Experiments were conducted under the following conditions: solar irradiance $I_{\text{solar}} = 1000\,\text{W}\,\text{m}^{-2}$, feed stream salinity equal to 35 g L^{-1} and inlet temperature of permeate and feed equal to 20 °C. The device was tested within a solar simulator box (PV Infinity Q4-14-C), which provides a stable and uniform light source mimicking solar irradiation. In detail, the simulator delivers a typical irradiance of 1000 W m^{-2}, with high spatial uniformity (<5%, <1% in the central area) and temporal stability (±10 W over 24 h). The light source is a metal-halide lamp, producing a broadband spectrum covering visible and near-infrared wavelengths. The irradiation level was calibrated using a pyranometer (Delta OHM LP PYRA 08) to ensure consistency. To maintain a temperature gradient across the membrane, a cooling plate (referred to as the heat exchanger in Fig. 1, see component 8) was installed beneath the module. Cooling water at approximately 27 ± 3 °C (depending on environment conditions over the testing period), supplied by a commercial chiller (CW-3000), was circulated through the plate. Note that the CW-3000 is an air-cooled passive unit that relies on convective heat dissipation to the surrounding environment, without active refrigeration. Temperature measurements were recorded using a National Instruments cDAQ-9174 data acquisition system. Thermocouples placed in compression fittings measured inlet and outlet temperatures of both channels, while additional RS PRO Type K thermocouples monitored external top and bottom surface temperatures. Feed and permeate inlet temperatures were actively controlled via a thermostatic bath (Julabo Corio CD-300F). Mass flow rates were regulated using a peristaltic pump (Leadfluid BT100s). Both feed and permeate loops operated as closed hydraulic circuits, with buffer volumes maintained in beakers for fluid recirculation. Distillate production was quantified by monitoring the increase in permeate mass over time using precision balances (Radwag PS1000.R2 and Kern PCB). To assess water quality and detect potential salt leakage, permeate conductivity was continuously measured with a conductivity meter (Chauvin Arnoux C.A 10141). In addition, the salinity of both the feed and permeate streams was verified at the beginning and at the end of the experiment using a digital refractometer (Hanna HI 96821).

2.2.1. *Experimental procedure for the testing*

All experiments were conducted following a standardized procedure to ensure consistent and repeatable testing conditions across all configurations. First, the device was filled with distilled water on the permeate side and artificial seawater on the feed side. Once the module was fully charged and prepared, the solar simulator was activated. After approximately 30 min of continuous irradiation, the device typically reached steady-state condition. At the point, the experiment proceeded for an additional 60 min, yielding a total duration of around 1.5 h. Throughout the test, the inlet temperatures for both the feed and permeate channels were maintained at the target values using the temperature controller, and the chiller remained operational to ensure consistent cooling.

2.3. *Numerical model*

To support the understanding of the heat and mass transfer behavior of the prototype, a numerical model was developed using the Finite Element Method (FEM) in COMSOL Multiphysics©. The model is formulated under steady-state conditions and assumes a two-dimensional geometry (see Fig. 4). The simulation domain includes the feed and permeate channels (both with height of 2.60 mm) as well as the membrane, but excludes the spacers. Although neglecting spacers may slightly underestimate productivity (≈7%, at most), this simplification, in addition to being conservative from an engineering perspective, is justified by the relatively low flow rates considered, which make their impact negligible. In fact, the flow remains laminar and aligns smoothly along the spacer surface without generating significant wakes, so spacer-induced turbulence is minimal.

Heat transfer is solved across the entire computational domain. Then, fluid flow in the feed and permeate channels is governed by the Navier–Stokes equations. In the feed channel, solute transport is modeled using the advection–diffusion equation, allowing for the local resolution of salt concentration and accurate computation of water activity α at the membrane interface, necessary for evaluating the effective vapor pressure gradient. The membrane is modeled as a porous solid. Mass transfer through the membrane is simulated using a coupled Maxwell–Stefan and dusty-gas model, based on standard assumptions widely adopted in membrane distillation literature [18,19]. Thermal transport within the membrane is treated as conduction through a solid layer, with interfacial heat sources incorporated to represent phase change phenomena. Additional modeling details are provided and discussed in the following section.

2.3.1. *Main governing equations*

The fluid flow in the feed and permeate channels is governed by the steady-state Navier–Stokes momentum equation, under incompressible flow assumptions:

$$\rho\bar{u}\cdot\nabla\bar{u} = -\nabla p + +\mu\nabla^2\bar{u} + f \tag{1}$$

where $\bar{u}$ is the fluid velocity vector, ρ is the fluid density, p is the fluid pressure, μ is the fluid dynamic viscosity, and f represents body force per unit volume. Then, to properly compute the vapor flux through the membrane, knowledge of the salt concentration at the membrane-solution interface is required. Therefore, the steady-state advection-diffusion transport equation for salt is implemented:

$$\bar{u}\cdot\nabla c = D\nabla^2 c + S \tag{2}$$

where c is the salt concentration of feed aqueous solutions, D is the molecular diffusion coefficient of salt, and S is the source/sink term accounting for local effects. Heat transfer within the channels is modeled by:

$$\bar{u}\cdot\nabla T = \frac{k}{c_p\rho}\nabla^2 T + \frac{q}{c_p\rho} \tag{3}$$

where T is the temperature, k is the thermal conductivity, c_p is the specific heat capacity, and q indicates any volumetric heat generation.

2.3.2. *Mass transfer across the membrane*

Mass transfer through the membrane was modeled using a combination of the Maxwell–Stefan and Dusty-Gas models, which describe multicomponent diffusion in porous media [18]. In this framework, the molar flux N_i of species i is governed by:

$$-\frac{x_i}{RT}\frac{d\mu_i}{dz} = \frac{x_i K_v}{\eta_v \epsilon_m D_{iK}}\frac{dp}{dz} + \sum_{\substack{j=1\\ j\neq i}}^{n}\left(\frac{x_j N_i - x_i N_j}{\frac{p\epsilon D_{ij}}{RT\tau}}\right) + \frac{N_i}{\frac{p\epsilon D_{iK}}{RT\tau}} \tag{4}$$

where x_i is the mole fraction of species i, μ_i is the chemical potential, D_{ij} is the binary diffusion coefficient, D_{iK} is the Knudsen diffusion coefficient, K_v is the viscous permeability, η_v is the dynamic viscosity,

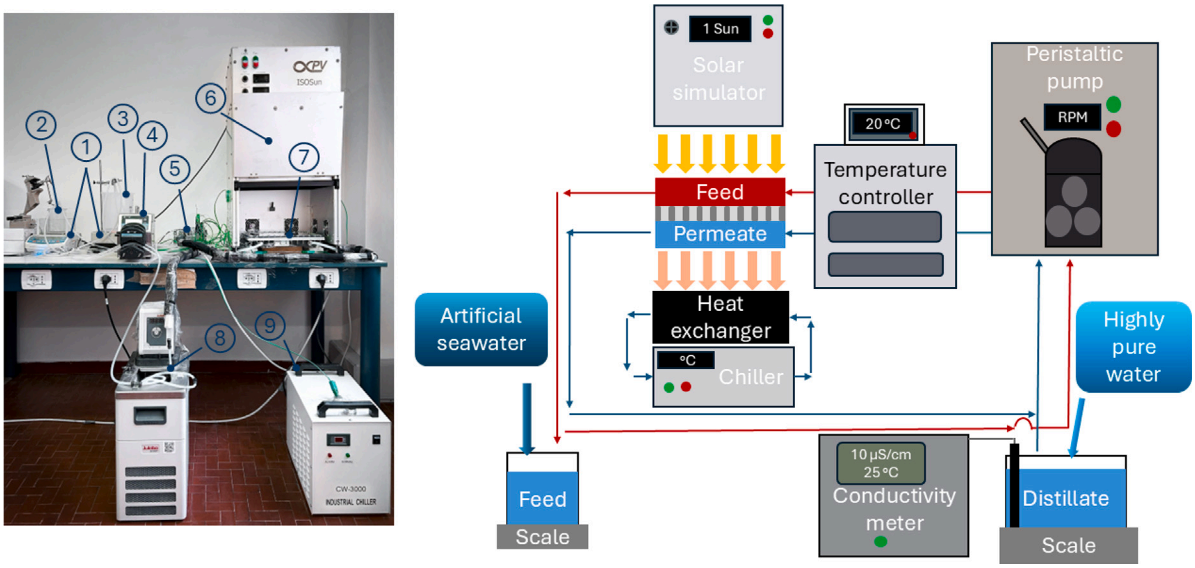

Fig. 3. Experimental setup used for MD module testing and characterization. The figure on the left shows the actual components used: (1) precision scales for monitoring the mass evolution over time, (2) permeate beaker, (3) feed beaker, (4) peristaltic pump for controlling the mass flow rate, (5) data acquisition system, (6) solar simulator for mimicking solar irradiation, (7) custom-designed MD module, (8) thermostatic bath (temperature controller) for setting the desired inlet temperature and (9) chiller, which acts as the heat sink. The figure on the right illustrates the schematic of the setup including the fluidic circuit.

ϵ is the membrane porosity, τ is the tortuosity, and p is the absolute pressure. To simplify Eq. (4), several assumptions can be safely considered and introduced, as reported extensively in literature [18,19]. First, it was assumed that the total pressure gradient across the membrane is negligible, i.e., $\frac{dp}{dz} = 0$, which eliminates the contribution of the viscous flow term. Second, the gas phase inside the membrane pores was treated as a binary ideal mixture of water vapor and air only. Lastly, the system is assumed to follow ideal gas behavior [30]. Under this assumption, the chemical potential of water vapor can be expressed as:

$$\mu_w = \mu_w^{\circ} + RT\ln(x_w) \tag{5}$$

With these assumptions, Eq. (4) reduces to (for extensive details see Ref. [18]):

$$-\frac{dx_w}{dz} = \frac{x_a N_w}{\frac{p\epsilon D_{wa}}{RT\tau}} + \frac{N_w}{\frac{p\epsilon D_{wK}}{RT\tau}} \tag{6}$$

Integrating the expression across the membrane thickness from the evaporating surface (referred as E) to condensation surface (referred as C), and defining the specific mass flux $J = M_{H_2O}N_w$, we get:

$$J = \frac{M_{H_2O}\, p\, \epsilon\, D_{wa}}{RT\,\tau\, h} \ln\left(\frac{1 - x_w^C + \frac{D_{wa}}{D_{wK}}}{1 - x_w^E + \frac{D_{wa}}{D_{wK}}}\right) \tag{7}$$

Since for our purposes $x_w \ll 1$, the equation can be linearized via first-order Taylor expansion (for extensive details see Ref. [18]), leading to the final used form:

$$J = K\,\Delta p_v \tag{8}$$

where the membrane permeability coefficient K is expressed as:

$$K = \left(\frac{RT\, p_a\, \tau\, h}{\epsilon\, M_{H_2O}\, p\, D_{wa}} + \frac{RT\,\tau\, h}{M_{H_2O}\, D_{wK}\, d_p}\right)^{-1} \tag{9}$$

with d_p being the average pore diameter, h the membrane thickness, $D_{wK} = \frac{d_p}{3}\sqrt{\frac{8RT}{\pi M_{H_2O}}}$ the Knudsen diffusion coefficient [30], $\tau = \frac{(2-\epsilon)^2}{\epsilon}$ the estimated tortuosity, D_{wa} the binary diffusion coefficient of water vapor in air, and p_a the partial pressure of air. The product $p\,D_{wa}$ varies with temperature [18,19] as:

$$p\,D_{wa} = 1.19\times10^{-4}\,T^{1.75} \tag{10}$$

Then, the driving force Δp_v is defined as:

$$\Delta p_v = \alpha(Y_F)\,p_v(T_F) - \alpha(Y_P)\,p_v(T_P) \tag{11}$$

where $p_v(T)$ is the saturation pressure of pure water at temperature T, and $\alpha(Y)$ is the water activity, calculated as [18]:

$$\alpha = \frac{M_{\mathrm{NaCl}}(1-Y)}{M_{\mathrm{NaCl}}(1-Y) + N_{ion}M_{H_2O}Y} \tag{12}$$

where M_{NaCl} is the molar mass of the NaCl, N_{ion} is the number of ions and $Y = \frac{m_{\mathrm{NaCl}}}{m_{solution}}$ is the mass fraction of salt.

2.3.3. *Heat transfer across the membrane*

The membrane was modeled as a solid with an effective thermal conductivity given by:

$$k_m = (1-\epsilon)k_{air} + \epsilon\, k_{PTFE} \tag{13}$$

where k_{air} is the thermal conductivity of air trapped in the membrane pores, and k_{PTFE} the thermal conductivity of the PTFE. The total heat flux through the membrane ϕ includes both sensible (namely, heat conduction accounted for via the Fourier model) and latent heat transfer contributions:

$$\phi = \frac{k_m}{h}\Delta T + J\;\Delta h_v \tag{14}$$

where $\Delta T = T_{m,f} - T_{m,p}$ is the temperature difference across the membrane, being $T_{m,f}$ and $T_{m,p}$ the feed and permeate temperature at the membrane-solution interfaces, and Δh_v is the latent heat of vaporization.

2.3.4. *Boundary conditions*

The boundary conditions applied to the simulated control volume are summarized in Fig. 4, which refers specifically to configuration PF. However, the boundary conditions are generally consistent across all configurations, with only minor variations. In CF, the direction of the feed mass flow is reversed. As discussed, in $CF_{f,\ closed-loop}$, the only difference lies in the feed inlet temperature. For $CF_{heat\ recovery}$ configuration, it is assumed that the temperature of the feed stream entering the upper feed channel equals the outlet temperature of the underlying preheating channel (namely $T_{f,T} = T_{f,B}$, see Fig. 2d). This assumption neglects any heat loss or gain between the preheater outlet and the module inlet, potentially leading to a slight underestimation of the actual feed temperature at the module entrance, and thus a slight underestimation of system performance.

With regard to the boundary conditions for the species transport advection-diffusion equation (see Eq. (2)), these are not shown in Fig. 4 to avoid overloading the graphical representation, but are detailed as follows. At the inlet of the feed channel, the salt concentration is set to 35 g L^{-1}. At the membrane interface, local salt accumulation due to the evaporative flux is accounted for by applying mass balance-based boundary conditions. On the opposite impermeable wall (namely, feed stream - aluminum interface), a no-flux condition is imposed, while at the outlet of the feed channel, a zero-gradient condition is applied for salt concentration.

Heat transfer from the lateral surfaces of the MD module to the surrounding environment, as shown by the red lines in Fig. 4, is modeled using the expression $\phi = U_{amb}(T - T_{amb})$. The global heat transfer coefficient U_{amb} is evaluated as $U_{amb} = (\frac{1}{L_g/k_g} + \frac{1}{h_{air}})^{-1}$ where k_g is the thermal conductivity of the sealing gasket, L_g is its longitudinal dimension, h_{air} is the convective heat transfer coefficient between the module surfaces and the surrounding environment. Under experimental conditions within the solar simulator box, h_{air} was estimated as 48 ± 5 W m^{-2} K^{-1}, primarily due to the presence of forced convection from internal fans. For simulations replicating realistic field conditions, a lower value of $h_{\mathrm{air}} = 5$ W m^{-2} K^{-1} was assumed to reflect natural convection.

Similarly, the heat transfer coefficient for the polycarbonate plate is defined as $U_{poly} = (\frac{1}{L_p/k_p} + \frac{1}{h_{air}})^{-1}$, where L_p is the thickness of the polycarbonate plate and k_p its thermal conductivity. The ambient temperature T_{amb} inside the solar simulator was measured to be approximately 40 °C, while for simulations representing realistic outdoor conditions, it was set to 25 °C. For clarity, we note that throughout the manuscript the simulations performed under the experimental solar-simulator conditions (i.e., $T_{amb} = 40$ °C and $h_{\mathrm{air}} = 48 \pm 5$ W m^{-2} K^{-1}) are labeled in the figures as *Model prediction*, whereas the simulations using outdoor-representative boundary conditions (i.e., $T_{amb} = 25$ °C and $h_{\mathrm{air}} = 5 \pm 5$ W m^{-2} K^{-1}) are labeled as *Field simulation*. This nomenclature is used consistently in all results figures. The heat sink placed at the bottom of the module is modeled according to $\phi_{heat\ sink} = U_{sink}(T - T_{sink})$, where U_{sink} and T_{sink} were experimentally determined. Specifically, U_{sink} was measured as 660 W m^{-2} K^{-1} and T_{sink} was found to be 27 ± 3 °C under sun simulator conditions and 25 °C under field conditions. The temperature T_{sink}, representing the temperature of the cooling water circulating through the metal heat exchanger, was monitored throughout all experiments and incorporated into the numerical model.

Finally, to reconcile experimental temperature measurements with the numerical model inlet conditions, a temperature correction was applied. In the experimental setup, the temperature is measured at a thermowell located a short distance upstream of the actual device inlet. This positioning is due to practical constraints related to sensor placement and sealing, requiring the thermocouple to be located inside a thermowell upstream of the device inlet. However, because of this offset, the fluid experiences additional heat exchange between the thermowell and the physical inlet of the device, typically resulting in a slightly higher effective temperature by the time it reaches the membrane module. To account for this temperature rise, an analytical correction model was developed and applied in the numerical simulations. The model assumes steady-state, one-dimensional heat transfer along a cylindrical pipe segment (here, a silicone tube) connecting the thermowell to the device inlet. The governing equation for the mean fluid temperature $T_m(x)$ is expressed as [31]:

$$\frac{dT_m}{dx} = \frac{\pi\ D_{in}}{\dot{m}\ c_p} U_{HTC}(T_\infty - T_m) \tag{15}$$

Here, D_{in} is the inner diameter of the pipe, $\dot{m}$ is the mass flow rate, c_p is the specific heat capacity of the fluid, T_∞ is the ambient temperature, and U_{HTC} is the overall heat transfer coefficient between the fluid and the surroundings. The coefficient U_{HTC} incorporates the thermal resistance of the pipe material (e.g., silicone) and the convective heat transfer coefficients on both the internal (fluid side) and external (air side) surfaces. It thus depends on factors such as pipe wall thickness, thermal conductivity of the tube, fluid velocity, and ambient airflow. By solving Eq. (15) with appropriate boundary conditions, the fluid temperature at the physical module inlet is estimated and subsequently used as the inlet boundary condition in the numerical model. This correction ensures greater consistency between the experimental measurements and the simulated thermal behavior.

2.4. Water quality assessment

Water quality was evaluated by measuring the electrical conductivity of the collected water before and after the test. It is important to distinguish between distillate and the permeate. In this context, distillate refers to the total water volume accumulated in the beaker, which includes both the initial distilled water used to fill the system (device and piping) and the water that permeated through the membrane during the experiment. Permeate, on the other hand, specifically refers to the vapor that crossed the membrane and condensed during the test period. Since the system is initially filled with pure distilled water, the newly produced permeate becomes diluted, particularly in short-duration tests, potentially leading to an overestimation of salt rejection if not corrected. To account for this dilution effect, the actual salt concentration of the permeate was estimated by comparing the electrical conductivity of the distillate before and after the test, and correlating it with the permeate volume produced, as shown in Eq. (16) [32–34]:

$$C_p = \frac{k_{EC} \times (EC_d \times V_d - EC_{d,i} \times V_{d,i})}{V_p} \tag{16}$$

where C_p is the estimated salt concentration of the permeate produced during the test, $k_{EC} = 0.50$ [32–34] is the empirical correlation coefficient between salt concentration and electrical conductivity, EC_d and $EC_{d,i}$ are the electrical conductivities of the total distillate volume at the end and start of the test, respectively, V_d and $V_{d,i}$ are the corresponding distillate volumes, and V_p is the volume of vapor that permeated through the membrane. Electrical conductivity measurements were normalized to a reference temperature of 25 °C using the following correction equation:

$$EC_{ref} = \frac{EC_d}{1 - \alpha_{EC} \times (T_{ref} - T_d)} \tag{17}$$

where EC_{ref} is the electrical conductivity at the reference temperature being 25 °C, $\alpha_{EC} = 0.055$ is the temperature coefficient, T_{ref} is the temperature reference and T_d is the temperature of the distilled volume [32–34].

Finally, the salt rejection ratio R, a key indicator for evaluating water quality, was calculated as:

$$R = 1 - \frac{C_p}{C_{feed}} \tag{18}$$

where C_{feed} is the salt concentration of the feed solution.

2.5. Additional parameters for performance evaluation

A key parameter for evaluating system performance is the thermodynamic efficiency defined as:

$$\eta = \frac{J A_m \Delta h_v}{I_{solar} A_c} \tag{19}$$

where A_m is the effective membrane area (26 × 26 cm), A_c is the solar absorber area of the module (36 × 36 cm), and I_{solar} is the solar

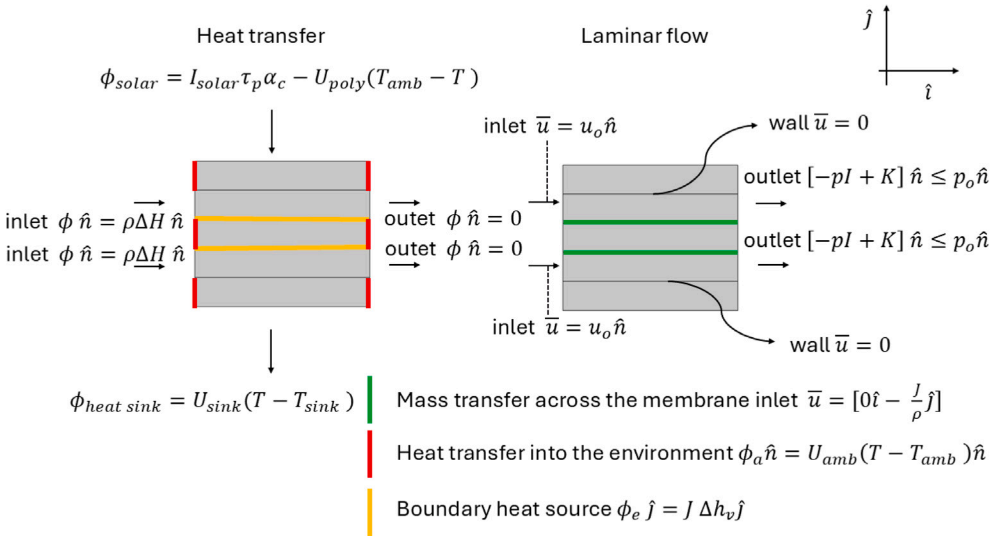

Fig. 4. The figure illustrates the boundary conditions applied in the numerical model for configurations PF. Red lines indicate heat transfer toward the environment, while the green lines indicate mass transfer across the membrane. ϕ_{solar} represents the net solar irradiation entering the system. The term τ_p and α_c denote the transparency of the polycarbonate and the absorption coefficient of the coating, respectively. The heat flux directed toward the heat sink is represented by the term $\phi_{heat\ sink}$.

irradiation (1000 W m^{-2}). In these expressions, J is the distillate flux expressed in kg m^{-2} s^{-1}. Finally, the recovery factor is defined as:

$$RF = \frac{J\ A_m}{\dot{m}_f} \tag{20}$$

where $\dot{m}_f$ is the feed mass flow rate, expressed in kg s^{-1}.

3. Results

3.1. Main results

Fig. 5a summarizes the distilled water production achieved under optimal operating conditions for each configuration, within the tested range of operating parameters. These experiments were conducted under controlled laboratory conditions, with both inlet temperatures initially set to 20 °C and no external heating applied, unless otherwise stated.

Configurations PF and CF served as reference cases (see Fig. 2, panel a and b). Both configurations demonstrated optimal performance at a mass flow rate of 5.60 mL min^{-1} (corresponding to a fluid velocity of 1.2×10^{-4} m s^{-1}). Under these conditions, the experimentally measured specific productivity J was 0.32 ± 0.01 kg m^{-2} h^{-1} for both PF and CF (see Fig. 5a). These values represent the mean slope of linear fits applied to the time-resolved mass increase in the permeate beaker, obtained from $n = 3$ independent experiments. Each linear regression yielded a minimum R^2 of 0.998, and the reported uncertainty corresponds to the standard deviation (±1 s.t.d.). Numerical predictions closely matched the experimental results, yielding J values of 0.32 ± 0.03 kg m^{-2} h^{-1} and 0.32 ± 0.04 kg m^{-2} h^{-1} for PF and CF respectively. This excellent agreement confirms the reliability of the numerical model. It is interesting to notice that, although counter-current flow configurations are widely recognized in the literature for enhancing performance under standard operating conditions, particularly when the feed inlet temperature is significantly higher than the permeate inlet, the advantage becomes negligible under the specific conditions of this study. Here, both inlet temperatures are low (near to ambient) and nearly equal, and heating is provided exclusively through distributed solar energy. As a result, configuration CF does not show a significant increase in specific productivity compared to PF. This behavior is further discussed and quantitatively analyzed in the following section.

Following the analysis of the reference configurations, the alternative setup $CF_{f,\ closed-loop}$ was investigated, wherein the feed-side circuit was thermally closed. This configuration is identical to CF in all aspects except for the thermal management of the feed stream. Specifically, the feed tank served as a passive thermal reservoir, allowing the feed temperature to increase gradually rather than being actively maintained at 20 °C. The temperature rise depends on the mass flow rate: at 5.60 mL min^{-1}, it increases by 4.40 ± 0.14 °C; at 28.50 mL min^{-1}, by 7.20 ± 0.46 °C; and at 56.60 mL min^{-1}, by 10.90 ± 0.59 °C. These values represent the mean ± 1 s.t.d. The observed increase with flow rate is attributed to heat exchange with the ambient environment along the circuit segment between the module and the feed beaker. Note that the observed increase in feed temperature is strongly influenced by the thermal insulation of the fluidic circuit, which has not been optimized in the current setup. As a result, the extent of this effect may vary and could potentially be higher. This represents an engineering challenge that may be addressed through improved insulation in future designs.

$CF_{f,\ closed-loop}$ configuration resulted in slightly increased performance at lower flow rates and a more pronounced improvement at higher flow rates, compared to baseline configuration. The highest productivity for this configuration, shown in Fig. 5, was again observed at 5.60 mL min^{-1}, with a measured J of 0.36 ± 0.03 kg m^{-2} h^{-1} (see Fig. 5a). It is worth noting that, although higher flow rates lead to a greater overall temperature rise as previously quantified, optimal performance is still achieved at a lower mass flow rate. Numerical simulations indicate that at a mass flow rate of 5.60 mL min^{-1}, the average temperature difference across the membrane is 1.41 °C, with a mean membrane temperature (calculated as the average of vector $\frac{T_{m,f}(x)+T_{m,p}(x)}{2}$) of 32.37 °C. In contrast, at a mass flow rate of 56.60 mL min^{-1}, the temperature difference slightly decreases to 1.38 °C, and the mean membrane temperature drops to 31.26 °C.

Then, configuration $CF_{heat\ recovery}$ (see Fig. 2, panel d), which was designed to enhance thermal efficiency by reducing heat loss to the environment through the heat sink (namely one of the primary sources of thermal loss), was tested at the mass flow rate of 28.50 mL min^{-1}, as predicted to be optimal by simulations. Experimentally, this configuration achieved the highest productivity of 0.51 ± 0.02 kg m^{-2} h^{-1} (see Fig. 5a), primarily due to the combined effects of feed preheating and permeate cooling. This value represents the mean slope of linear fits applied to the time-resolved mass increase in the

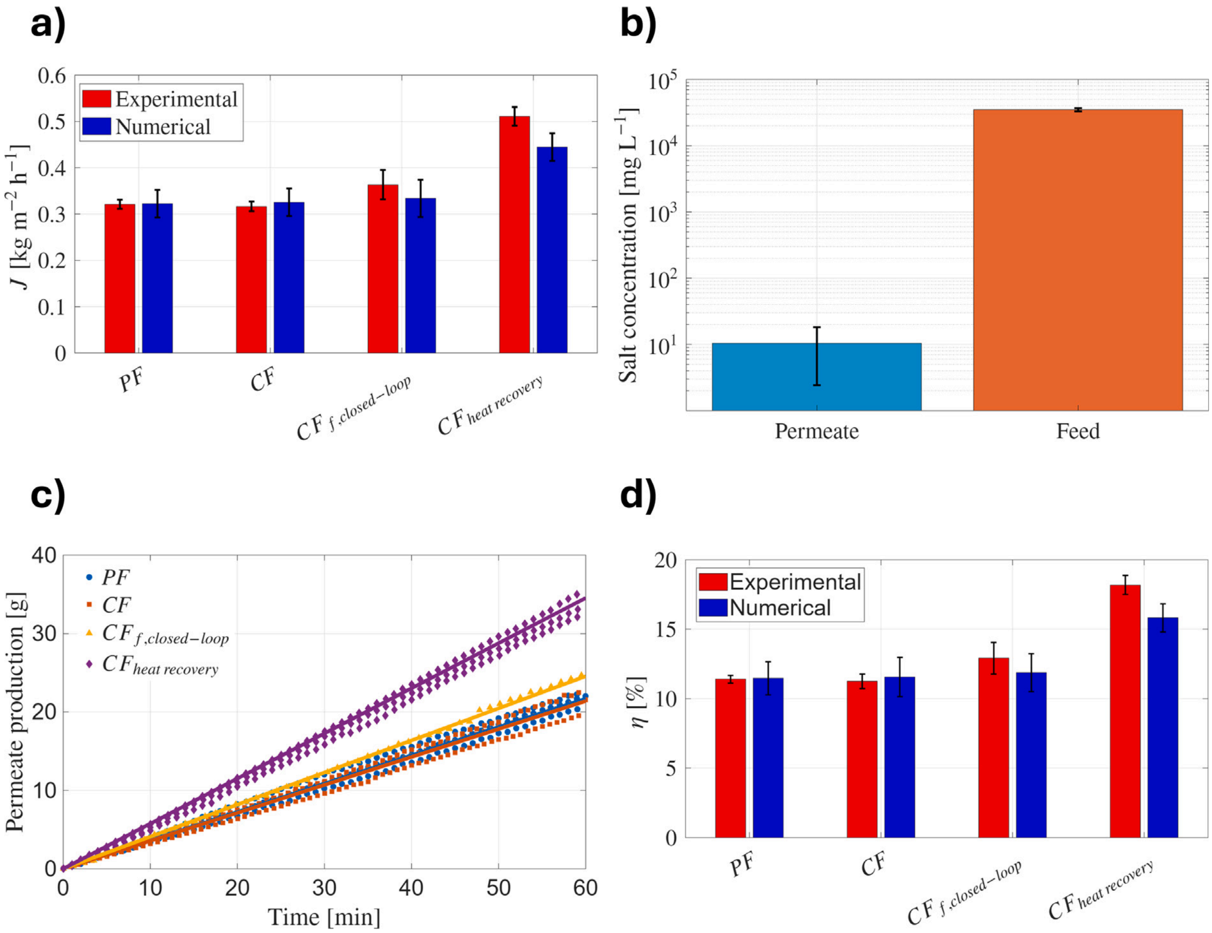

Fig. 5. Optimal performance results for each configuration within the tested parameter range. (a) Highest specific distillate productivity (J) achieved in each configuration; red and blue bars represent experimental and numerical values, respectively. (b) Salt concentrations, expressed in mg/L, measured in the permeate and feed basins for $CF_{heat\ recovery}$, the tested configuration with the highest productivity. (c) Cumulative permeate production over time. The solid line represents the average mass evolution trend, while each dot corresponds to experimental data collected at steady state. Different colors represent the different tested configurations: purple for $CF_{heat\ recovery}$, yellow for $CF_{f,\ closed-loop}$, and orange and blue for CF and PF, respectively. (d) Thermodynamic efficiency of each configuration at its optimal operating point.

permeate beaker, obtained from $n = 3$ independent experiments. Each linear regression yielded a minimum R^2 of 0.996, and the reported uncertainty corresponds to the standard deviation (namely 1 ± 1 s.t.d.).

Water quality was assessed for all configurations by estimating the salt concentration (C_p) from electrical conductivity measurements by using Eq. (16). As shown in Fig. 5b, the salt concentration decreased by approximately four orders of magnitude, from $35{,}000 \pm 2000$ mg/L to 20 ± 16 mg/L (mean and standard deviation over three experiments), corresponding to a salt rejection R exceeding 99.9%. For brevity, salt concentration data are reported only for the configuration exhibiting the highest distilled water productivity; however, C_p remained consistently below 40 mg/L in all tests conducted.

In addition, panel (c) of Fig. 5 shows the cumulative distilled water production over time, as directly measured by high-precision scale placed on the permeate side, for each of the tested configurations. Both the raw experimental data and the corresponding linear fitting lines are shown to highlight the steady-state production rates. The linear trends observed after an initial stabilization phase indicate that all configurations operate under steady-state conditions. As expected, configurations with improved thermal management, such as $CF_{f,\ closed-loop}$ and $CF_{heat\ recovery}$, show steeper slopes, reflecting higher production rates. In contrast, reference cases PF and CF exhibit lower slopes, in line with their more limited thermal efficiency.

Finally, the thermodynamic efficiency of the investigated configurations, evaluated at their respective optimal mass flow rates and shown in Fig. 5d, ranged from 11% to 18%. The highest efficiency, 18%, was achieved by $CF_{heat\ recovery}$. The recovery factor (RF) varied between 2% and 7%, with the peak value observed in $CF_{f,\ closed-loop}$. Although $CF_{heat\ recovery}$ achieved the highest overall productivity, its optimal operating point required a higher mass flow rate, resulting in a comparatively lower recovery factor.

3.2. Parametric analysis of device performance

3.2.1. Baseline configurations

The baseline configurations investigated, PF and CF, are analyzed to evaluate performance across a range of mass flow rates and feed inlet temperatures. Specifically, PF was experimentally tested under various mass flow rates, while CF was experimentally examined only at the optimal mass flow rate predicted by numerical simulations. Both configurations have been extensively studied numerically with respect to the effects of mass flow rate and feed inlet temperature. Fig. 6(a) shows the specific distillate productivity J as a function of mass flow rate for configuration PF, which was also selected for numerical model validation. The gray shaded area represents the model prediction range under solar simulator conditions, accounting for uncertainties in membrane thickness ($h = 0.18 \pm 0.05$ mm, as reported by producer) and sink temperature ($T_{sink} = 27 \pm 3$ °C). The black solid line represents the mean prediction, while red markers denote experimental data obtained under the same solar simulator conditions. The numerical

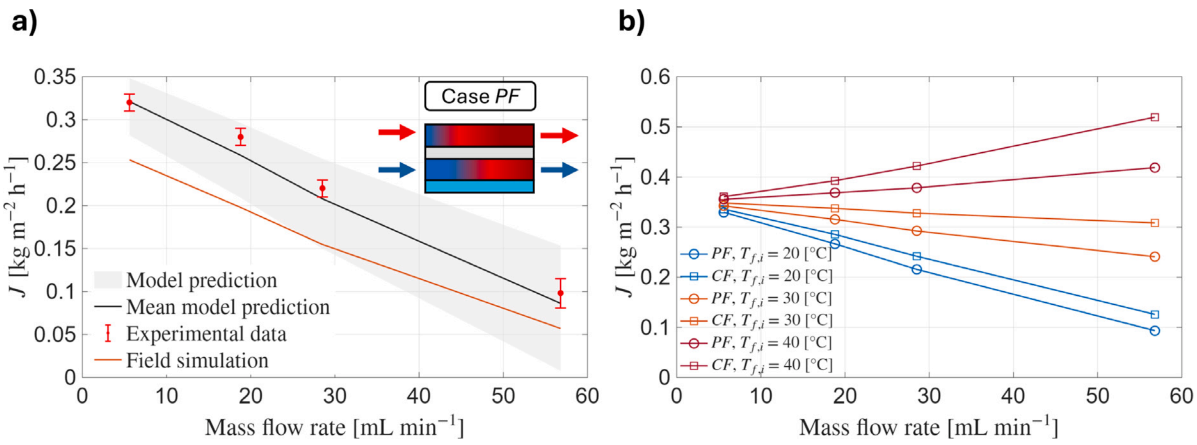

Fig. 6. Device performance for baseline configuration under standard operating conditions (35 g L^{-1}, I_{solar} = 1000 W m^{-2}, permeate inlet temperature set to 20 °C). (a) Specific distillate productivity J as a function of mass flow rate for case PF. The black line indicates the mean numerical prediction, with the gray shaded region indicating the uncertainty due to variations in membrane thickness (h) and sink temperature (T_{sink}). Red markers with error bars denote experimental results obtained under solar simulator conditions. The orange solid line corresponds to the numerical prediction under representative field conditions, where T_{amb} and T_{sink} are fixed at 25 °C, and the convective heat transfer coefficient (h_{air}) is set to 5 W m^{-2} K^{-1}. (b) Numerical predictions of J as a function of mass flow rate for both configurations (PF and CF) at varying feed inlet temperatures.

model shows good agreement with experimental results across all tested flow rates, yielding a mean absolute error below 12%. This consistency supports the reliability of the developed model in capturing the dominant transport phenomena across the full range of operating conditions. For comparison and completeness, the orange solid line shows model predictions under representative field conditions, where ambient and sink temperatures (T_{amb} and T_{sink}) are set to 25 °C and the air heat transfer coefficient (h_{air}) is fixed at 5 W m^{-2} K^{-1}. Under these conditions, productivity for PF decreases by 22%, from 0.32 to 0.25 kg m^{-2} h^{-1} at the optimal mass flow rate (namely 5.60 mL min^{-1}), primarily due to increased convection heat losses. Both configurations (PF and CF) reach maximum productivity at a mass flow rate of 5.60 mL min^{-1} (see Fig. 6, panel b), with an experimental value of J = 0.32±0.01 kg m^{-2} h^{-1} for both cases. Beyond this flow rate, J decreases monotonically, which is due to enhanced streamwise advection, which limits the feed temperature rise during its residence time in the MD module. Indeed, since both the feed and permeate streams enter at 20 °C, higher flow rates reduce residence time, thereby diminishing the transmembrane temperature difference and associated distillate flux. In quantitative terms, for configuration PF, increasing the flow rate from 5.60 to 18.80 mL min^{-1} results in approximately 12.50% decrease in J (from 0.32±0.01 kg m^{-2} h^{-1} to 0.28±0.03 kg m^{-2} h^{-1}). This highlights the sensitivity of specific productivity to residence time under isothermal inlet conditions.

Configuration CF, which inverts the permeate flow direction to form a counter-flow arrangement, is commonly employed in MD systems [13]. As mentioned before, this configuration is typically advantageous at higher inlet feed temperatures (50–80 °C), higher flow rates and in systems lacking distributed direct solar heating [35], as it maximizes the temperature gradient across the membrane. However, under isothermal inlet conditions (20 °C for both streams), and low mass flow rates, the performance difference between PF and CF remains minor. For instance, at 5.60 mL min^{-1}, the relative difference in specific productivity J is less than 2%, indicating that the flow configuration has a negligible effect under these conditions.

Numerical simulations (see Fig. 6b) were conducted to further investigate the influence of feed inlet temperature on the transmembrane vapor flux across a range of mass flow rates. For both configurations, at low flow rates (5.60 mL min^{-1}), preheating the feed from 20 °C to 30 °C and 40 °C results in relatively modest productivity increases of 3.70% and 7.80%, respectively. In contrast, the impact becomes substantial at higher flow rates, with productivity gains of 145% and 348% for the same temperature increments.

Moreover, among the two configurations, CF consistently exhibits superior performance relative to PF at higher flow rates and under increasing feed temperatures. In detail CF achieved improvements of up to 28% and 24% at inlet feed temperature equal to 30 °C (orange lines in Fig. 6b) and 40 °C (red lines in Fig. 6b), respectively. These findings highlight the greater suitability of CF for operating conditions involving feed preheating. Accordingly, all subsequent configurations involving thermal input (i.e., feed inlet temperatures above 20 °C) adopt CF as the baseline design.

3.2.2. Configuration $CF_{f,\ closed-loop}$

The other configuration analyzed, referred to as case $CF_{f,\ closed-loop}$, differs from the previous cases in that the thermostatic bath controlling the feed circuit is deactivated. As a result, the feed inlet temperature is no longer fixed at 20 °C but instead increases naturally due to the thermally closed-loop design of the fluidic circuit. This passive heating can enhance system performance, although the extent of the improvement is strongly dependent on the mass flow rate (see Fig. 7).

At a low mass flow rate of 5.60 mL min^{-1}, the feed inlet temperature increases by only 4.40 ± 0.14 °C, resulting in a modest experimental performance gain of approximately 10%, from 0.32±0.01 kg m^{-2} h^{-1} in PF (see Fig. 6) to 0.36±0.03 kg m^{-2} h^{-1} in $CF_{f,\ closed-loop}$ (see Fig. 7). In contrast, at a higher flow rate of 56.60 mL min^{-1}, the feed temperature increases by 10.9 ± 0.58 °C, leading to a substantial experimental productivity improvement: J rises from 0.098 ± 0.02 kg m^{-2} h^{-1} in PF (see Fig. 6) to 0.29 ± 0.1 kg m^{-2} h^{-1}, corresponding to an increase of approximately 185%.

Interestingly, at a mass flow rate of 5.60 mL min^{-1}, a productivity of 0.36±0.03 kg m^{-2} h^{-1} is achieved, despite a lower feed inlet temperature compared to the case at 56.60 mL min^{-1}, where the productivity is 0.29 ± 0.10 kg m^{-2} h^{-1}. As previously discussed, this counterintuitive result is supported by numerical simulations: at 5.60 mL min^{-1}, the average temperature difference across the membrane is 1.41 °C, with a mean membrane temperature, evaluated along the module, of 32.37 °C. At 56.60 mL min^{-1}, both values decrease slightly, with an average temperature difference of 1.38 °C and a mean temperature of 31.26 °C.

It should be noted that in this regime, the experimental uncertainty increased, as test replicates were conducted on different days. This is primarily due to the sensitivity of this configuration to ambient temperature fluctuations, which affect the performance of the chiller used to cool the permeate (see Fig. 3).

Fig. 7 also presents simulation results under realistic field conditions (see orange line). At 5.60 mL min^{-1}, the flux decreases to

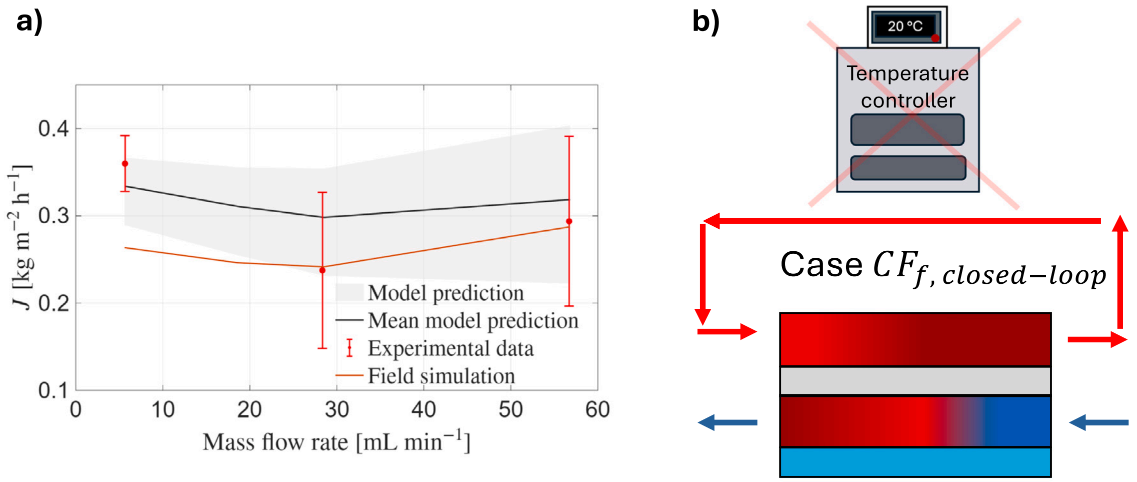

Fig. 7. Experimental and numerical results for configuration $CF_{f,\ closed-loop}$. Experiments were conducted using artificial seawater with a salinity of 35 g L^{-1}, under constant solar irradiation (I_{solar} = 1000 W m^{-2}) and a fixed permeate inlet temperature of 20 °C. (a) Specific distillate productivity (J) as a function of mass flow rate. The black line represents the mean numerical prediction, and the gray shaded area indicates the uncertainty range associated with variations in feed inlet temperature (T_{feed}), cooling temperature (T_{sink}), and membrane thickness (h). Experimental data are shown as red markers with error bars indicating standard deviation. The orange solid line corresponds to the numerical prediction under representative field conditions, where T_{amb} and T_{sink} are fixed at 25 °C, and the convective heat transfer coefficient is set to (h_{air} = 5 W m^{-2} K^{-1}). (b) Schematic of the tested configuration, showing the deactivation of the thermostatic bath in the closed-loop feed circuit.

0.26 kg m^{-2} h^{-1}, while at 56.60 mL min^{-1}, it remains comparable at 0.29 kg m^{-2} h^{-1}. This behavior reflects a balance between two opposing effects: increased convective thermal losses are offset by a lower sink temperature. In the field scenario, the sink temperature T_{sink} is fixed at 25 °C, enhancing the driving temperature gradient across the membrane. For comparison, the lab condition at 56.60 mL min^{-1} featured a higher T_{sink} of 27 ± 3 °C.

3.2.3. Configuration $CF_{heat\ recovery}$: internal heat recovery enabled by novel layered flow design

The final configuration, denoted as $CF_{heat\ recovery}$ (see Fig. 2, panel d), introduces an interesting passive thermal management strategy designed to maximize thermal efficiency without requiring any additional external thermal energy input. In this setup, the aluminum cooling plate, the external heat exchanger and the chiller are removed. Instead, a PTFE insulating plate is positioned at the bottom of the device to limit thermal losses, and a promising three-layer fluidic architecture is implemented. From top to bottom, the device comprises: (i) a feed flow channel exposed to direct solar irradiation, (ii) a permeate flow channel, and (iii) an auxiliary feed channel located beneath the permeate (see Fig. 2, panel d). The feed initially enters the auxiliary feed channel at upstream temperature equal to 20 °C, where it acts as a heat sink, cooling the permeate stream above. After exiting this channel, the feed, having absorbed heat from the permeate, enters the uppermost feed chamber in a preheated state. This simple rearrangement enables internal heat recovery, improving the effective temperature gradient across the membrane and system performance. Extensive numerical simulations were conducted to evaluate the performance of this configuration. Fig. 8a shows the modeled J values as a function of mass flow rate. The gray shaded area represents the numerical prediction interval, while the solid black line indicates the mean model prediction. Unlike the baseline cases, $CF_{heat\ recovery}$ exhibits a non-monotonic performance trend, with J increasing, peaking, and then decreasing as flow rate varies. The non-monotonic behavior observed arises from a trade-off between residence time (which favors heating and internal recovery) and advection/mixing (which reduces temperature polarization). Specifically, at low feed/permeate flow rates each fluid element receives more heat per unit mass from the auxiliary pre-heater and from the distributed solar absorber, increasing the bulk feed temperature. However, very low velocities promote thicker thermal boundary layers at the membrane, enhancing temperature polarization and reducing the effective membrane surface temperature on the feed side, an effect that limits vapor flux despite the high bulk temperature. At intermediate flow rates the competing effects are balanced: preheating remains effective while advective mixing is sufficient to keep boundary layers thin, producing the maximum flux. As flow rate increases further, advection becomes dominant and bulk temperature rise is suppressed because the fluid spends too little time under the distributed heat input; consequently productivity falls. It is worth observing that the location of the maximum shifts with solar flux, module length and channel thickness, parameters that can be tuned to move the optimum to desired operational ranges. This mechanistic understanding suggests clear optimization pathways for different application targets. Therefore, the validated numerical model predicts peak productivity at a mass flow rate of 28.50 mL min^{-1}, which corresponds experimentally to a specific distillate flux of $J = 0.51 \pm 0.02$ kg m^{-2} h^{-1} (mean and standard deviation over three experiments). This represents a 59% improvement over the best-performing reference configuration (namely PF and CF). This enhancement is particularly significant given that no additional thermal input is provided beyond distributed solar irradiation via the sun simulator. The experimental result (see red marker in Fig. 8a) closely aligns with the simulation (see gray shaded area in Fig. 8a), exceeding the mean predicted J value (see black solid line in Fig. 8a) by approximately 14%, thereby providing further validation of the conservative numerical approach. These minor discrepancies are attributed to simplifying modeling assumptions that slightly underestimate the feed temperature at the device top (see Section 2.3). A more precise local estimation of $T_{f,T}$ could in principle be obtained through a full 3D simulation; however, the associated computational cost would be substantial and unlikely to yield proportionally more in-depth physical insight for the scope of this study. For mass flow rates above or below 28.50 mL min^{-1}, performance declines monotonically. The decrease is more pronounced at lower flow rates, due to reduced advective transport and less effective permeate cooling. At higher flow rates, the drop is more gradual, likely caused by shorter residence times and reduced transmembrane temperature gradients. It worth noting that in the baseline scenario, the coolant velocity in the cooling plate (here replaced by the auxiliary feed channel) is orders of magnitude higher

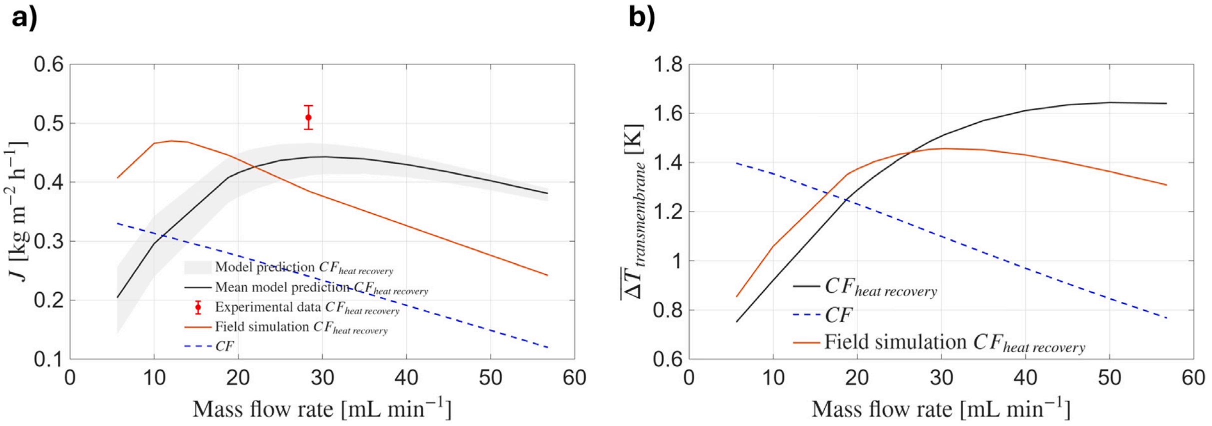

Fig. 8. (a) Specific distillate productivity (J) as a function of mass flow rate. The continuous black line represents the mean numerical prediction for $CF_{heat\ recovery}$, while the gray shaded area indicates the uncertainty range associated with membrane thickness (h), as reported by the manufacturer. The orange line corresponds to numerical results for $CF_{heat\ recovery}$ under field conditions, where T_{amb} and T_{sink} are fixed at 25 °C and h_{air} is set to 5 W m^{-2} K^{-1}. The blue dashed line shows the numerical prediction for configuration CF, included here for comparison with the baseline setup. (b) Average temperature difference across the membrane for configuration CF (blue dashed line), $CF_{heat\ recovery}$ (black solid line), and $CF_{heat\ recovery}$ under field conditions (orange solid line).

than the feed and permeate flow rates. For completeness, Fig. 8a also includes numerical predictions under representative field conditions (solid orange line). Under these conditions, optimal performance is predicted at a flow rate of 12 mL min^{-1}, yielding a productivity of 0.47 kg m^{-2} h^{-1}. Note how under realistic field conditions the maximum productivity (numerical) value achieved at 12 ml min^{-1} is higher than the maximum (numerical) value reached within the solar simulator at 28.50 mL min^{-1}. This is due to the higher average membrane temperature (49.08 °C compared to 38.41 °C), despite the slightly lower average membrane temperature difference, which decreases from 1.48 °C to 1.17 °C.

Notably, when the mass flow rate falls below approximately 20 mL min^{-1}, the module exhibits superior performance under representative field conditions compared to laboratory tests conducted under the solar simulator. This is primarily attributed to the significantly lower convective heat transfer coefficient in the field (5 W m^{-2} K^{-1}) compared to the controlled laboratory environment (48 W m^{-2} K^{-1}), which results in reduced thermal losses from the absorber to the surroundings. At low flow rates, the longer residence time, combined with lower heat losses under field conditions, results in a higher temperature gradient across the membrane and, consequently, higher vapor flux (see orange line in Fig. 8b, which refers to numerical average transmembrane temperature difference $\overline{\Delta T}_{transmembrane}$ as a function of mass flow rate). In contrast, at higher flow rates, the solar simulator environment yields superior performance. This is primarily due lower temperature of the surface absorber because of the increased advection, which facilitates more effective heat input from solar simulator environment. Under field conditions, although thermal losses to the environment remain minimal, the reduced residence time at elevated flow rates limits the extent of heat transfer to the fluid, thereby constraining performance.

For completeness, Fig. 8 also includes the transmembrane vapor flux and temperature difference $\overline{\Delta T}_{transmembrane}$ for CF, reported as a reference (dashed blue line). For flow rates exceeding 18.50 mL min^{-1}, $CF_{heat\ recovery}$ (black line) consistently exhibits a higher transmembrane temperature difference compared to CF, aligning with its superior productivity. Interestingly, $CF_{heat\ recovery}$ achieves higher vapor flux than CF even at flow rates below 18.50 mL min^{-1}, and starting from approximately 10 mL min^{-1}. This is attributed to the higher mean temperature across the membrane in $CF_{heat\ recovery}$. Specifically, at a flow rate of 10 mL min^{-1}, the numerical model predicts mean membrane temperatures of 49.40 °C for $CF_{heat\ recovery}$ and 32.12 °C for CF configuration, both under sun simulator conditions. The mean membrane temperature significantly influences vapor pressure, which follows an exponential dependence on temperature. It is also worth noting that the peak in J does not exactly coincide with the maximum $\overline{\Delta T}_{transmembrane}$, due to spatial averaging along the membrane and the nonlinear relationship between vapor flux and temperature gradient.

In summary, $CF_{heat\ recovery}$ showcases how a minimal yet strategic layout modification, routing the feed beneath the permeate before entering the main upper feed channel, enables effective internal heat recovery. This configuration substantially enhances distillate productivity without additional energy input, highlighting its potential for passive, energy-efficient desalination systems.

3.3. Comparative analysis with the state of the art

Finally, to better contextualize the performance of the proposed device, Fig. 9 compares its productivity with that of other compact MD systems powered solely by distributed solar energy and operating with feedwater at ambient temperature. Both the specific productivity (panel a; J, in kg m^{-2} h^{-1}) and the integral distillate production rate (panel b; g h^{-1}) are reported to enable a consistent comparison across different system scales and configurations.

The comparison includes three main categories of systems previously reported in the literature:

- Passive capillary-fed solar MD devices (in a blue color scale in Fig. 9): These compact, fully passive units integrate the solar absorber and the MD module, relying on capillary forces for feed transport. Single-stage devices typically achieve 0.48–1.20 kg m^{-2} h^{-1} [18,19,36,37], while multistage configurations (up to 10 stages) can reach 3 [18]–5.80 [37] kg m^{-2} h^{-1}. Other interesting multistage prototypes considered in the analysis, were proposed by Wang group [38,39]. However, the overall size of such devices is limited (≤15 cm) by capillary-driven flow, which constrains total throughput and scalability. Our single stage prototype achieves comparable specific productivity (0.51 kg m^{-2} h^{-1}) while being actively circulated and thus more scalable.
- Photothermal membrane distillation (PTMD) active systems (in a orange color scale in Fig. 9): PTMD modules employ photothermal coatings or nanostructured surfaces to localize heating at the membrane–feed interface, thereby mitigating temperature polarization and enhancing evaporation efficiency. Several configurations have been reported in the literature. For instance, Lienhard and co-authors conducted one of the first experimental demonstrations of an AGMD system with direct membrane heating [26]. Subsequently, Wu et al. developed a DCMD configuration using photothermal nanocomposite membranes [40].

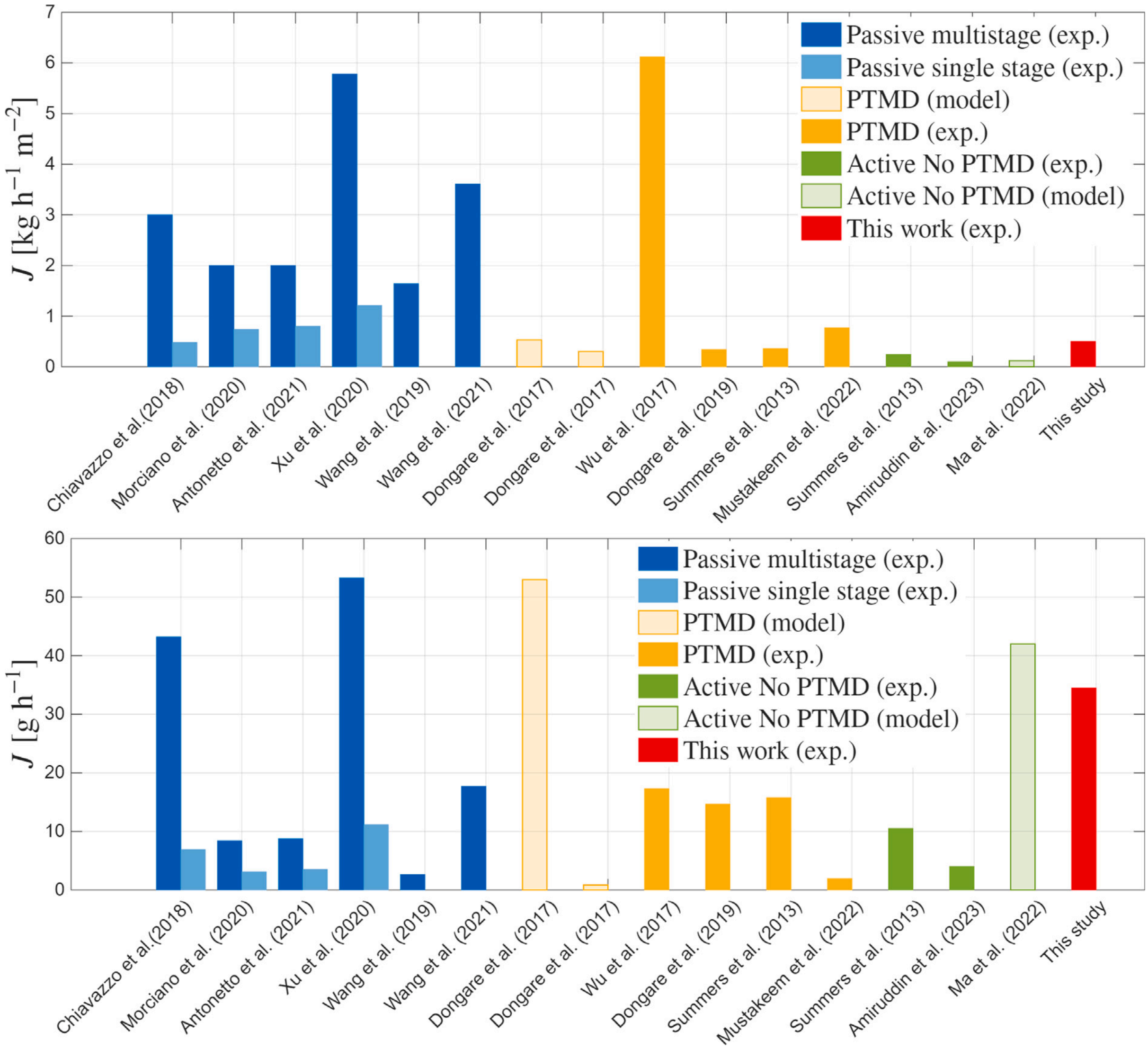

Fig. 9. Comparative analysis of the present distributed-solar MD prototype against existing compact passive and active solar-driven MD systems reported in the literature, under similar conditions. Both specific productivity (J, in kg m^{-2} h^{-1}) and integral distillate production rate (g h^{-1}) are shown. Color codes indicate system typology: blue = passive capillary-fed MD; green = compact active distributed-heating MD; orange = compact active photothermal MD; red = present work.

More recently, Halas and co-workers explored nanophotonics-enabled solar membrane distillation for off-grid desalination [24], as well as optical concentration using lens arrays to generate localized hot spots and boost vapor flux [41]. Finally, in 2022, Mustakeem et al. introduced MXene-coated membranes for solar-driven desalination [42]. While these PTMD systems have demonstrated the potential of localized photothermal heating, they face challenges related to coating durability, fabrication complexity, and large-scale manufacturability. Among the reported studies, the best-performing devices, those from the Halas group [24], achieved simulated fluxes of approximately 0.53 kg m^{-2} h^{-1} and total distillate production up to 53 g h^{-1}. These values are comparable to the experimentally demonstrated performance of the present work (0.51 kg m^{-2} h^{-1} and 35 g h^{-1}), yet obtained here through a simpler, coating-free design that inherently offers greater scalability and robustness.

- Active compact MD systems (in a green color scale in Fig. 9): To overcome the size and flow limitations of passive configurations, a few recent studies, most closely aligned with the our present approach (reported as a red bar in Fig. 9), have proposed active MD prototypes that integrate internal solar absorption while operating at very low feed velocities, typically orders of magnitude lower than those in conventional MD modules. It is worth stressing that these systems eliminate the need for external heat exchangers for feed preheating, relying instead on solar energy distributed and absorbed directly within the module. However, the available literature on such compact active devices remains scarce. Most reported systems are either purely numerical or rely on vacuum-assisted operation, which requires additional energy input. Instead, representative examples include the works by Lienhard et al. [26] and Ma et al. [27], which reported fluxes in the range of 0.10–0.12 kg m^{-2} h^{-1} under comparable boundary conditions. More recently, Amiruddin et al. [28] demonstrated a compact AGMD prototype achieving ~0.10 kg m^{-2} h^{-1} at ambient feed temperature, further confirming the competitiveness of our results. Nevertheless, such AGMD designs face scalability challenges, as their performance depends on gravity-driven permeate drainage and precise device inclination. In contrast, the present system, actively circulated yet compact and passively heated, offers greater design flexibility and scalability potential while maintaining comparable or superior performance under low-grade thermal conditions.

Within this framework, the proposed compact MD prototype distinguishes itself by operating without vacuum assistance, photothermal coatings, or external preheating, relying solely on distributed solar energy and an internal heat-recovery mechanism (introduced here for the first time) that passively couples the feed and permeate channels. This design effectively bridges the gap between passive devices, which offer relatively high specific productivity but limited scalability, and active configurations, which are more scalable but complex. The resulting system provides a simple, energy-efficient solution for low-grade heat utilization, with negligible electrical pumping energy (on the order of 10^{-4} kWh m^{-3}, as confirmed by pressure-drop experimental measurements at representative flow rates). Looking ahead, scaling this concept to a multistage configuration may further enhance total productivity, as supported by previous passive multistage solar distillation trends [18, 36] and by the comparatively high single-stage productivity (in absolute production rate) observed here under comparable low-temperature conditions.

A preliminary, order-of-magnitude cost assessment was also performed to contextualize the prototype within broader landscape of MD technologies. Based on bulk or shelf (when available) material prices, explicitly excluding manufacturing and scale-up effects, the material cost of 1 m^2 of the current prototype is estimated to lie between 63 and 167 USD m^{-2}, depending on whether non-optimized or reduced-thickness components are considered. Assuming a 10-year lifetime, annual operational costs, and 8 h of daily operation, this corresponds to a rough Levelized Cost of Water (LCOW) of approximately 7–18 USD m^{-3}. These values fall within the broad range reported for MD systems, which varies significantly with scale, heat-source configuration, and system integration. For instance, Amaya et al. [43] reported LCOW values between 1 and 10 USD m^{-3} depending on plant size. Choi et al. [44] found LCOW values as high as 56.50 USD m^{-3} for a solar-driven MD pilot plant. Usman et al. [45] reported costs ranging from 1.6 to 6.8 USD m^{-3} for MD systems utilizing combinations of waste heat, solar energy, and grid electricity. Given the simplified assumptions of this preliminary estimate and the omission of manufacturing and economy-of-scale effects, these figures should be interpreted only as indicative. A rigorous techno-economic analysis will be required as part of future system-scale development.

4. Discussions and conclusions

This work presents the design, development, and testing of a custom MD prototype that exclusively uses distributed solar energy as its thermal input. The system is engineered to maximize thermal coupling through reduced channel thicknesses, allowing solar energy to be directly absorbed into the feed stream without relying on external heating or active control mechanisms. Solar energy is collected via a planar integrated collector composed of a polycarbonate cover and an aluminum plate in thermal contact with a commercial spectrally selective solar absorber. The feed flows in direct contact with the heated aluminum plate, establishing the temperature gradient necessary for membrane distillation.

The key contribution of this study lies in the extensive experimental and numerical validation of a sustainable method for supplying thermal energy to the MD unit via direct, distributed solar heating along the feed channel, a strategy recently proposed in the literature to mitigate temperature polarization, yet still lacking systematic experimental exploration. This work contributes new insights by (i) exploring a broader range of operating conditions (i.e., particularly low unexplored mass flow rates rarely analyzed in conventional MD literature) offering a new perspective on how distributed solar input can be effectively harnessed and by (ii) developing a CFD model capable of accurately predicting the system's behavior. The developed CFD model demonstrated good agreement with experimental results, providing a predictive tool for future optimization of system parameters.

Although the distillate productivity is lower than that of conventional MD systems, improving maximum output was not the primary aim of this work. Rather, the architecture proposed in this study focuses on demonstrating how solar-driven, quasi-passively operated configurations can be optimized for simplicity, modularity, and compatibility with renewable energy sources. The system is therefore not intended to compete directly with conventional high-throughput desalination technologies (e.g., high-pressure reverse osmosis or high-temperature MD), but to offer an alternative, low-complexity approach tailored to decentralized, off-grid applications where autonomy and passive operation are prioritized. These features, together with the demonstrated performance under low inlet temperature conditions highlights the system's ability to efficiently harness distributed solar heat, making it particularly relevant for small-scale, off-grid and resource-limited desalination applications.

Building on this framework, we introduced a novel passive internal heat recovery strategy in which the feed stream is routed below the permeate channel before entering the main feed channel. This layout enables both internal preheating of the feed and cooling of the permeate, enhancing the effective transmembrane temperature difference without requiring additional external components for cooling or energy input. The proposed configuration achieved a specific distillate productivity of $J = 0.51 \pm 0.02$ kg m^{-2} h^{-1} under laboratory conditions with standard solar irradiation, representing a substantial improvement (59%) compared to single-stage MD with distributed energy and no internal preheating setups.

Future investigations should consider longer membrane modules, as the uniformly distributed thermal input may support more extended geometries without the typical thermal degradation observed in conventional designs. Beyond solar applications, the modular and thermally passive architecture of the device makes it a suitable candidate for integration with waste heat sources, such as photovoltaic panels or industrial surfaces. Finally, from a scalability perspective, the modular design proposed in this work offers significant flexibility in deployment. The optimal module length should first be determined based on the specific operating and boundary conditions, taking into account the distributed solar absorption that mitigates temperature decay along the feed channel. During this optimization phase, scaling up to larger membrane areas will require careful consideration of flow distribution and pressure drop constraints. Once the optimal geometry is identified, the system can be most effectively scaled out through replication of compact modules operated hydraulically in parallel. These modules can function as independent units, maintaining low pressure losses and simple hydraulic connections, while also allowing for potential thermal interconnection to enhance heat recovery in larger installations.

Overall, this study provides a controlled proof-of-concept validation of a solar-driven MD configuration under repeatable laboratory conditions, establishing the foundation for field implementation. Looking ahead, research will focus on extensive outdoor testing of the prototype under real solar irradiation, variable weather conditions, and different feedwater salinities to evaluate long-term stability, fouling behavior, and material durability. These studies, planned for the upcoming campaign, will reduce the gap between controlled laboratory assessment and real-world operation. In parallel, extended endurance tests using feedwater with higher scaling propensity will be conducted to evaluate the robustness of salt rejection and system stability under repeated thermal cycling. Further efforts will explore multistage configurations and optimized heat management strategies aimed at improving both energy efficiency and freshwater yield in decentralized desalination scenarios.

CRediT authorship contribution statement

Stefan Morosanu: Writing – review & editing, Writing – original draft, Visualization, Validation, Methodology, Investigation, Formal analysis, Data curation. **Matteo Morciano:** Writing – review & editing, Writing – original draft, Visualization, Validation, Supervision, Resources, Project administration, Methodology, Investigation, Funding acquisition, Formal analysis, Conceptualization.

Declaration of competing interest

The authors declare that they have no known competing financial interests or personal relationships that could have appeared to influence the work reported in this paper.

Acknowledgments

This work is part of the PNRR-NGEU project, funded by the Italian Ministry of University and Research (MUR) under Ministerial Decree No. 117/2023. The project has also been co-funded by Green Independence S.R.L., whose support is gratefully acknowledged. Authors would also like to thank Alessandro Monticelli, CEO of Green Independence S.R.L., for his valuable support in the design and prototyping of the module.

Data availability

Research Link Provided

Raw experimental data (Original data) (Zenodo)

References

[1] C. He, Z. Liu, J. Wu, X. Pan, Z. Fang, J. Li, B.A. Bryan, Future global urban water scarcity and potential solutions, Nat. Commun. 12 (1) (2021) 4667.
[2] F. Dolan, J. Lamontagne, R. Link, M. Hejazi, P. Reed, J. Edmonds, Evaluating the economic impact of water scarcity in a changing world, Nat. Commun. 12 (1) (2021) 1915.
[3] E.R. Jones, M.F. Bierkens, M.T. van Vliet, Current and future global water scarcity intensifies when accounting for surface water quality, Nat. Clim. Chang. 14 (6) (2024) 629–635.
[4] N. Akhtar, M.I. Syakir Ishak, S.A. Bhawani, K. Umar, Various natural and anthropogenic factors responsible for water quality degradation: A review, Water 13 (19) (2021) 2660.
[5] Ş. Kılkış, G. Krajačić, N. Duić, M.A. Rosen, et al., Effective mitigation of climate change with sustainable development of energy, water and environment systems, 2022.
[6] Z.M. Ghazi, S.W.F. Rizvi, W.M. Shahid, A.M. Abdulhameed, H. Saleem, S.J. Zaidi, An overview of water desalination systems integrated with renewable energy sources, Desalination 542 (2022) 116063.
[7] Ş. Kılkış, G. Krajačić, N. Duić, M.A. Rosen, et al., Accelerating mitigation of climate change with sustainable development of energy, water and environment systems, 2021.
[8] I. SHC, A fundamental look at supply side energy reserves for the planet, Sol. Update 62 (2015).
[9] A.O. Maka, J.M. Alabid, Solar energy technology and its roles in sustainable development, Clean Energy 6 (3) (2022) 476–483.
[10] V.R. Moreira, J.V. Raad, J.X. Lazarini, L.V. Santos, M.C. Amaral, Recent progress in membrane distillation configurations powered by renewable energy sources and waste heat, J. Water Process. Eng. 53 (2023) 103816.
[11] B. Tashtoush, W. Alyahya, M. Al Ghadi, J. Al-Omari, T. Morosuk, Renewable energy integration in water desalination: State-of-the-art review and comparative analysis, Appl. Energy 352 (2023) 121950.
[12] A.S. Jawed, L. Nassar, H.M. Hegab, R. van der Merwe, F. Al Marzooqi, F. Banat, S.W. Hasan, Recent developments in solar-powered membrane distillation for sustainable desalination, Heliyon 10 (11) (2024).
[13] S. Shalaby, A. Kabeel, H. Abosheiasha, M. Elfakharany, E. El-Bialy, A. Shama, R.D. Vidic, Membrane distillation driven by solar energy: A review, J. Clean. Prod. 366 (2022) 132949.
[14] Q. Li, L.-J. Beier, J. Tan, C. Brown, B. Lian, W. Zhong, Y. Wang, C. Ji, P. Dai, T. Li, et al., An integrated, solar-driven membrane distillation system for water purification and energy generation, Appl. Energy 237 (2019) 534–548.
[15] S.T. Bouguecha, S.E. Aly, M.H. Al-Beirutty, M.M. Hamdi, A. Boubakri, Solar driven dcmd: Performance evaluation and thermal energy efficiency, Chem. Eng. Res. Des. 100 (2015) 331–340.
[16] F. Mahmoudi, D. Ng, K. Ang, Z. Xie, Sustainable desalination through hybrid photovoltaic/thermal membrane distillation: Development of an off-grid prototype, Sol. Energy 284 (2024) 113090.
[17] Q. Ma, Z. Xu, R. Wang, Distributed solar desalination by membrane distillation: Current status and future perspectives, Water Res. 198 (2021) 117154.
[18] E. Chiavazzo, M. Morciano, F. Viglino, M. Fasano, P. Asinari, Passive solar high-yield seawater desalination by modular and low-cost distillation, Nat. Sustain. 1 (12) (2018) 763–772.
[19] G. Antonetto, M. Morciano, M. Alberghini, G. Malgaroli, A. Ciocia, L. Bergamasco, F. Spertino, M. Fasano, Synergistic freshwater and electricity production using passive membrane distillation and waste heat recovered from camouflaged photovoltaic modules, J. Clean. Prod. 318 (2021) 128464.
[20] V. Volkov, B. Bulushev, A. Ageev, Determination of the capillary size and contact angle of fibers from the kinetics of liquid rise along the vertical samples of fabrics and nonwoven materials, Colloid J. 65 (4) (2003) 523–525.
[21] R.R. Meo, M. Provenzano, M. Morciano, Investigating the solute concentration in capillary-fed vapor generators: A heat and mass transfer study, Int. Commun. Heat Mass Transfer 148 (2023) 106998.
[22] M. Gao, C.K. Peh, F.L. Meng, G.W. Ho, Photothermal membrane distillation toward solar water production, Small Methods 5 (5) (2021) 2001200.
[23] A. Bamasag, E. Almatrafi, T. Alqahtani, P. Phelan, M. Ullah, M. Mustakeem, M. Obaid, N. Ghaffour, Recent advances and future prospects in direct solar desalination systems using membrane distillation technology, J. Clean. Prod. 385 (2023) 135737.
[24] P.D. Dongare, A. Alabastri, S. Pedersen, K.R. Zodrow, N.J. Hogan, O. Neumann, J. Wu, T. Wang, A. Deshmukh, M. Elimelech, et al., Nanophotonics-enabled solar membrane distillation for off-grid water purification, Proc. Natl. Acad. Sci. 114 (27) (2017) 6936–6941.
[25] I.A. Said, S. Wang, Q. Li, Field demonstration of a nanophotonics-enabled solar membrane distillation reactor for desalination, Ind. Eng. Chem. Res. 58 (40) (2019) 18829–18835.
[26] E.K. Summers, et al., Experimental study of thermal performance in air gap membrane distillation systems, including the direct solar heating of membranes, Desalination 330 (2013) 100–111.
[27] Q. Ma, A. Ahmadi, C. Cabassud, Comparative study of small-scale flat-plate direct contact membrane distillation and vacuum membrane distillation modules with integrated direct solar heating, Desalination 529 (2022) 115633.
[28] D. Amiruddin, D. Mahajan, D. Fang, W. Wang, P. Wang, B.S. Hsiao, A facile ultrapure water production method for electrolysis via multilayered photovoltaic/membrane distillation, Energies 16 (15) (2023) 5765.
[29] J. Hu, G. Zhu, A. Ronen, D. Jassby, Q. Li, P. Wang, W. Wang, W. Zhang, Interfacial heating in membrane distillation: Advances, optimization strategies, and industrial applications for desalination, Environ. Sci. Technol. (2025).
[30] I. Hitsov, T. Maere, K. De Sitter, C. Dotremont, I. Nopens, Modelling approaches in membrane distillation: A critical review, Sep. Purif. Technol. 142 (2015) 48–64.
[31] F.P. Incropera, D.P. Dewitt, T.L. Bergman, A.S. Lavine, Fundamentals of Heat and Mass Transfer, John Wiley & Sons, Inc., Hoboken, NJ, 2002, 981p.
[32] J.J. Barron, C. Ashton, The effect of temperature on conductivity measurement, Tsp 7 (3) (2005) 1–5.
[33] B.D. Thomas, T.G. Thompson, C.L. Utterback, The electrical conductivity of sea water, ICES J. Mar. Sci. 9 (1) (1934) 28–34.
[34] A.F. Rusydi, Correlation between conductivity and total dissolved solid in various type of water: A review, in: IOP Conference Series: Earth and Environmental Science, vol. 118, IOP publishing, 2018, 012019.
[35] J. Ravi, M.H.D. Othman, T. Matsuura, M.R. Bilad, T. El-Badawy, F. Aziz, A. Ismail, M.A. Rahman, J. Jaafar, Polymeric membranes for desalination using membrane distillation: A review, Desalination 490 (2020) 114530.
[36] M. Morciano, M. Fasano, S.V. Boriskina, E. Chiavazzo, P. Asinari, Solar passive distiller with high productivity and marangoni effect-driven salt rejection, Energy & Environ. Sci. 13 (10) (2020) 3646–3655.
[37] Z. Xu, L. Zhang, L. Zhao, B. Li, B. Bhatia, C. Wang, K.L. Wilke, Y. Song, O. Labban, J.H. Lienhard, et al., Ultrahigh-efficiency desalination via a thermally-localized multistage solar still, Energy & Environ. Sci. 13 (3) (2020) 830–839.
[38] W. Wang, Y. Shi, C. Zhang, S. Hong, L. Shi, J. Chang, R. Li, Y. Jin, C. Ong, S. Zhuo, et al., Simultaneous production of fresh water and electricity via multistage solar photovoltaic membrane distillation, Nat. Commun. 10 (1) (2019) 3012.
[39] W. Wang, Y. Shi, C. Zhang, R. Li, M. Wu, S. Zhuo, S. Aleid, P. Wang, Solar seawater distillation by flexible and fully passive multistage membrane distillation, Nano Lett. 21 (12) (2021) 5068–5074.
[40] J. Wu, K.R. Zodrow, P.B. Szemraj, Q. Li, Photothermal nanocomposite membranes for direct solar membrane distillation, J. Mater. Chem. A 5 (45) (2017) 23712–23719.
[41] P.D. Dongare, A. Alabastri, O. Neumann, P. Nordlander, N.J. Halas, Solar thermal desalination as a nonlinear optical process, Proc. Natl. Acad. Sci. 116 (27) (2019) 13182–13187.
[42] M. Mustakeem, J.K. El-Demellawi, M. Obaid, F. Ming, H.N. Alshareef, N. Ghaffour, Mxene-coated membranes for autonomous solar-driven desalination, ACS Appl. Mater. & Interfaces 14 (4) (2022) 5265–5274.
[43] D. Amaya-Vías, J.A. López-Ramírez, Techno-economic assessment of air and water gap membrane distillation for seawater desalination under different heat source scenarios, Water 11 (10) (2019) 2117.
[44] J. Choi, J. Cho, J. Shin, H. Cha, J. Jung, K.G. Song, Performance and economic analysis of a solar membrane distillation pilot plant under various operating conditions, Energy Convers. Manage. 268 (2022) 115991.
[45] H.S. Usman, K. Touati, M.S. Rahaman, An economic evaluation of renewable energy-powered membrane distillation for desalination of brackish water, Renew. Energy 169 (2021) 1294–1304.